

## DETERMINATION OF MASS OF IGR J17091-3624 FROM “SPECTRO-TEMPORAL” VARIATIONS DURING ONSET-PHASE OF THE 2011 OUTBURST

N. IYER<sup>1,2</sup> AND A. NANDI<sup>1</sup><sup>1</sup>Space Astronomy Group, SSIF/ISITE Campus, ISRO Satellite Centre, Outer Ring Road, Marathahalli, Bangalore, 560037, India and<sup>2</sup>Indian Institute of Science, Bangalore, 560012, India

AND

S. MANDAL<sup>3</sup><sup>3</sup>Indian Institute of Space Science and Technology, Trivandrum, 695547, India

Draft version May 12, 2015

## ABSTRACT

The 2011 outburst of the black hole candidate IGR J17091-3624 followed the canonical track of state transitions along with the evolution of Quasi-Periodic Oscillation (QPO) frequencies before it began exhibiting various variability classes similar to GRS 1915+105. We use this canonical evolution of spectral and temporal properties to determine the mass of IGR J17091-3624, using three different methods, viz: *Photon Index ( $\Gamma$ ) - QPO frequency ( $\nu$ ) correlation*, *QPO frequency ( $\nu$ ) - Time (day) evolution* and *broadband spectral modelling based on Two Component Advective Flow*. We provide a combined mass estimate for the source using a Naive Bayes based joint likelihood approach. This gives a probable mass range of  $11.8 M_{\odot} - 13.7 M_{\odot}$ . Considering each individual estimate and taking the lowermost and uppermost bounds among all the three methods, we get a mass range of  $8.7 M_{\odot} - 15.6 M_{\odot}$  with 90% confidence. We discuss the possible implications of our findings in the context of two component accretion flow.

**Keywords:** accretion, accretion disks — black hole physics — radiation mechanisms: non-thermal — X-rays: individual (IGR J17091-3624)

## 1. INTRODUCTION

The enigmatic Galactic black hole candidate IGR J17091-3624 underwent multiple outbursts in 1994, 2001, 2003 and 2007 before the recent one in February 2011 (in’t Zand et al. 2003; Revnivtsev et al. 2003; Capitanio et al. 2006, 2012). During the 2011 outburst, the source displayed state transitions like other outbursting black hole sources (Remillard & McClintock 2006; Nandi et al. 2012) from the Hard to Intermediate states (Pahari et al. 2011; Rodriguez et al. 2011; Capitanio et al. 2012; Iyer & Nandi 2013). It also showed presence of a state with characteristics similar to a ‘canonical’ soft state (Iyer & Nandi 2013) of other outbursting black hole sources. After evolving along the canonical track, it started to display a number of temporal variability classes similar to GRS 1915+105 (Altamirano et al. 2011). The presence of High Frequency QPO ( $\sim 66$  Hz) similar to GRS 1915+105 (Altamirano & Belloni 2012) and radio detections, albeit at the level of a few mJy (Rodriguez et al. 2011) in the Hard and the Intermediate states were also seen in this outburst.

The similarity to GRS 1915+105 triggered immense interest about the nature of this source. As of now, its precise location upto  $5''$  is known and possible optical and infrared counterparts have been identified (Bodaghee et al. 2012) within the *Chandra* error circle. The distance to the source, mass and orbital parameters of both objects in the binary are currently unknown. What is certainly known, is that IGR J17091-3624 is only the second black hole candidate to display a wide range

of temporal and spectral variations after GRS 1915+105, although at much lower (10 to 50 times) observed flux levels (Altamirano et al. 2011). More knowledge about IGR J17091-3624 should allow us then to make some meaningful comparisons between these two sources. Multiple attempts have been made before to determine the mass of IGR J17091-3624. These attempts have placed it anywhere between  $< 3 M_{\odot}$  (Altamirano et al. 2011) to  $< 15 M_{\odot}$  (Altamirano & Belloni 2012). Other attempts to estimate the mass are  $< 5 M_{\odot}$  (Rao & Vadawale 2012),  $9.13 \pm 2.25 M_{\odot}$  (Pahari et al. 2011), and  $\sim 6 M_{\odot}$  (Rebusco et al. 2012). The wide range of these estimates doesn’t enable us to even pin down whether the source is a massive stellar black hole binary or an exceptionally low mass black hole candidate.

In this paper, we attempt to make an estimate of the mass with tighter constraints using X-ray observations made during the rising phase of its 2011 outburst. Here, we discuss *three* different methods (two of which are independent of distance to the source) to estimate its mass. In the  $3^{rd}$  approach, we study the broadband (0.5 to 100.0 keV) spectrum using the two component advective flow (TCAF) model (Chakrabarti & Titarchuk 1995; Chakrabarti & Mandal 2006). We use these three estimates to put a limit on the mass of the central object. Finally, we also discuss the results obtained from our spectro-temporal analysis in the light of two different types of accretion flows i.e., a Keplerian disk (Shakura & Sunyaev 1973) on the equatorial plane, sandwiched by a sub-Keplerian flow (Chakrabarti & Titarchuk 1995; Chakrabarti & Mandal 2006; Wu et al. 2002; Smith et al. 2001, 2002, 2007; Cambier & Smith 2013) on both sides of the Keplerian

disk in the vicinity of an accreting black hole.

## 2. OBSERVATIONS AND ANALYSIS

We use archival data of observations made by the *RXTE*, *Swift* and *INTEGRAL* satellites for the 2011 outburst (from 06 Feb (MJD 55598.28) onwards). We restrict ourselves to the rising phase of the outburst, before the source entered into its enigmatic and unpredictable variability phase. In all, we analyze  $\sim 40$  days of data from these observatories.

### 2.1. *Swift* data reduction

We use the *XRT* data from the *Swift* suite of instruments. The *XRT* data consists of windowed timing mode observations, which reduces pile-up effects from the source. The maximum observed count rate is about 40 counts  $\text{s}^{-1}$ . This ensures that the *XRT* data is not piled up (Romano et al. 2006). We analyse these *XRT* data-sets by following the steps as given in the *XRT* manual<sup>1</sup>. For this purpose, we use *HEASoft* 6.15.1 and its associated *ftools* packages. We restrict ourselves to use events of *grade* 0-2, while extracting timing and spectral data. The source and background regions are extracted by selecting a circular region of diameter 40 pixels ( $\sim 90''$ ) from the data images. While doing spectral modelling, we found that the low energy spectrum (0.5 – 1.0 keV) of the *Swift XRT* data did not fit well and showed some excess in the soft state. This was due to uncertainty in position of the source in the binned pixels of WT mode<sup>2</sup>. By using position dependent *rmfs*<sup>3</sup> made for different probable positions of the source on the detector Y pixel, we accounted for this apparent excess in the soft spectrum (K. Page 2014, private communication). We use such position dependent *rmfs* for each of our *Swift XRT* data-sets.

### 2.2. *INTEGRAL* data reduction

We use the *IBIS/ISGRI* instrument (Lebrun et al. 2003) from the *INTEGRAL* suite. We extract spectral information from *ISGRI* by following the steps as given in their data reduction manual<sup>4</sup>. To obtain the spectrum, we use *OSA v 10.0* along with updated versions of the calibration and response files. The spectrum from *ISGRI* is rebinned in order to get more data points for modelling the spectrum (see Table 1). We extract spectral information from *ISGRI* only for those dates which have simultaneous *Swift* observations. This helps us to obtain broadband (0.5 – 100 keV) data for our spectral analysis. In all the data-sets that we use, IGR J17091-3624 is visible in the *ISGRI* detector with significance greater than  $7\sigma$ . However, owing to the low source flux, there is non-detection or very low significance detection in the *JEM-X* detector. Hence, we do not use any spectral data from *JEM-X*.

### 2.3. *RXTE* data reduction

We use the *PCU2* and *HEXTE* detector data of the *RXTE* satellite. However, as noted (Pahari et al. 2011;

Capitanio et al. 2012; Iyer & Nandi 2013), the observations made by *RXTE* before 23 Feb are contaminated due to the nearby LMXB NS source GX 349+2. We do use these contaminated observations for our timing analysis. Specifically, we use them to find the frequency of QPOs from the power density spectrum (PDS). The source GX 349+2 does not exhibit any QPO like features in its PDS. We investigated the observations carried out by the *JEM-X* payload onboard *INTEGRAL* on 11 Feb 2011 to ascertain this. Also, as noted by O'Neill et al. (2002); Agrawal & Bhattacharyya (2003) no QPOs have ever been found in GX 349+2, in spite of extensive searches carried out over all the spectral and temporal states of this LMXB. This leads us to believe that the QPO like features in the PDS obtained from *PCU2* data are indeed from IGR J17091-3624. We use only the non contaminated data from *PCU2* and *HEXTE* detector for our spectral analysis.

### 2.4. Temporal Analysis

The Power Density Spectrum (PDS) of all data-sets is computed in the energy bands afforded by the observing instruments, viz. *Swift XRT* (0.5 – 10.0 keV) and *RXTE PCA* (3.0 – 30.0 keV). The PDS are obtained using *GHATS v1.1*<sup>5</sup>, a customized IDL based timing package, which takes care of re-binning, Poisson noise subtraction and dead-time correction (Zhang et al. 1995) of the FFT data. Each of the PDS is made by using temporal data of bin size 3.52 ms (for *Swift XRT* data) and 0.244 ms (for *RXTE PCA* data). All observations are divided into segments of 128.0 s and a PDS is computed individually for each such segment. We then obtain the final PDS for an entire observation by averaging the PDS from each individual segment. Finally, we systematically search each averaged PDS for the presence of QPOs. A combination of Lorentzian features is used to model the PDS. We select only those QPO features which have a significance greater than  $3\sigma$  for our analysis. The Q-factor ( $\nu/\text{FWHM}$ ) of these selected QPOs is found to vary between 3 to 10. The rms power under the QPO varies in between 8% to 17% and the QPO frequencies are observed to increase with time from 0.055 Hz to  $\sim 5$  Hz (Shaposhnikov 2011; Pahari et al. 2011; Rodriguez et al. 2011; Iyer & Nandi 2013). We have modelled this evolution of QPO frequencies in §3.2. The error on QPO frequency is taken to be  $1\sigma$  deviation from its centroid frequency, which is obtained by scaling its FWHM.

### 2.5. Spectral Analysis

The spectral analysis is carried out using *XSPEC v12.8.1g*. We do spectral modelling for individual observations of each instrument. Apart from this we also analyse broadband spectra (0.5 keV to 100.0 keV) as obtained by choosing *simultaneous observations* from *Swift XRT* and *INTEGRAL IBIS*. We rebin the spectrum obtained from each instrument and add systematic errors as mentioned in Table 1 before fitting the data-sets. We model the energy spectrum by two different methods. The first method (see Capitanio et al. 2012; Iyer & Nandi 2013) is a phenomenological model fitting of the spectrum and consists of a *diskbb* and a *powerlaw* (or *cutoffpl*) component. In this phenomenological modelling, we find that

<sup>1</sup> Swift XRT Data Reduction Guide, v1.2, 2005

<sup>2</sup> <http://www.swift.ac.uk/analysis/xrt/digest.cal.php#abs>

<sup>3</sup> <http://www.swift.ac.uk/analysis/xrt/rmfs.php>

<sup>4</sup> IBIS Analysis User Manual, Chernyakova, M. et al., 2012, ISDC

<sup>5</sup> <http://www.brera.inaf.it/utenti/belloni/GHATS.Package/Home.html>

the `powerlaw` photon index ( $\Gamma$ ) increases with time and is positively correlated with the QPO frequencies obtained in §2.4. We model this correlation as presented in §3.1 to obtain the source mass. We use  $1\sigma$  errors on fit parameters as estimated from the `XSPEC error` command for our model fitting routines. In the second method of spectral modelling, we calculate a model spectrum for each broadband observation using Two Component Advective Flow (TCAF). This is done by including radiative hydrodynamics of the accreting plasma self-consistently into the governing equations of the flow (Chakrabarti & Titarchuk 1995; Chakrabarti & Mandal 2006). We then use this calculated spectrum to fit the observed spectrum, which is presented in §3.3.

### 3. MODELS AND RESULTS

We consider three different approaches to estimate mass of the central source. These methods are discussed in the following sub-sections: spectro-temporal correlation (§3.1), the evolution of QPO frequencies (§3.2) and broadband spectral modelling (§3.3). Then, we use these three different estimates to derive a single set of bounds for the mass. The estimates are made under the TCAF paradigm (Chakrabarti & Titarchuk 1995), which enables us to model both evolution of spectral and temporal features under a single paradigm, thereby ensuring consistency of the estimate. In this paper, we have used radial distance in units of Schwarzschild radius ( $r_g$ ) and mass in units of solar mass ( $M_\odot$ ).

#### 3.1. Photon Index ( $\Gamma$ ) - QPO frequency ( $\nu$ ) correlation

A model for the observed correlation between the spectral fitted photon index ( $\Gamma$ ) and the observed QPO frequency ( $\nu$ ) for black hole candidates is presented in Titarchuk & Fiorito (2004). Shaposhnikov & Titarchuk (2007) (hereafter ST07) have presented an implicit empirical scaling relation between the correlation curves of different black hole sources and used it to estimate the mass of a few such sources. The model uses a ‘Compton cloud’ around the central source and a transition layer / region between this Compton cloud and the Keplerian disk. Any change in the size of the cloud leads to a change in both the QPO frequency (explained as the magneto-acoustic resonance oscillations of the bounded transition layer (Titarchuk & Wood 2002)) and the photon index of the emitted spectrum ( $\Gamma$ ) (due to varying optical depth of the hot electrons). We believe that the ‘Compton cloud’ in this model is the same as the post-shock region of the accretion disk under the TCAF paradigm (Chakrabarti & Titarchuk 1995). The TCAF paradigm too demonstrates both the steepening of spectral index and the increase in QPO frequencies with time (Chakrabarti et al. 2008; Nandi et al. 2012; Radhika & Nandi 2014; Debnath et al. 2014). In addition, the accretion disk configuration used in Titarchuk & Wood (2002); Titarchuk & Fiorito (2004) is similar to that under the TCAF paradigm. We thus expect the empirical correlation of ST07 should hold under the TCAF paradigm as well.

The correlation is fitted using the empirical relation given in ST07 :

$$\Gamma(\nu) = A - DB \ln \left[ \exp \left( \frac{\nu_{tr} - \nu}{D} \right) + 1 \right], \quad (1)$$

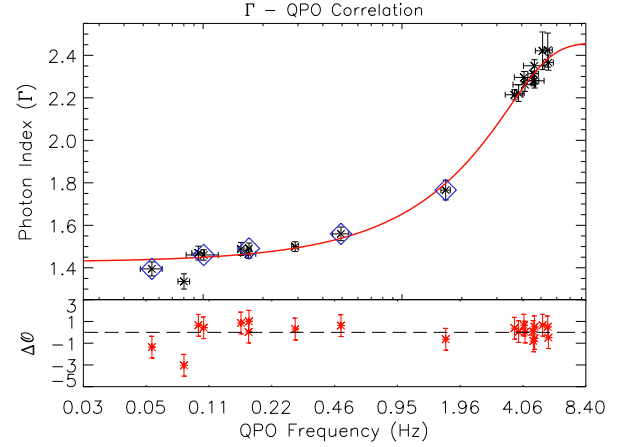


**Figure 1.** Photon index ( $\Gamma$ ) - QPO frequency ( $\nu$ ) correlation plot. Diamond points (blue) are *Swift XRT* QPOs. Rest of the QPO frequencies are from *RXTE PCA*. Bottom panel shows the weighted residuals in each point. The weights are assigned as given in Appendix I. The best fit curve (red solid line) using Eqn. 1 gives mass to be  $10.90_{-1.48}^{+1.67} M_\odot$ .

where A is the value at which the photon index saturates,  $\nu_{tr}$  is the threshold frequency above which the levelling off/saturation of  $\Gamma$  happens and B is the slope of the correlation which scales with mass. The parameter D controls how fast (i.e., over what frequency range) the transition occurs. We note that this is an empirical scaling equation relating the shape of the correlation curve with the masses of different black hole systems. To find the mass of an unknown source requires comparison of its correlation curve with a reference curve of a source with known mass. An inherent assumption in this scaling equation is the similarity of the shape of the correlation curves between these two sources (see also Shaposhnikov & Titarchuk 2009). The slope of this correlation curve, as the source transits from low photon index and frequency values in the harder states to the higher saturated photon index and frequency values of the softer states, is related to the mass of the source. The empirical scaling relation estimates this slope and a comparison of slopes from different sources gives a direct comparison of their masses. We consider the rising phase of the 2005 outburst of GRO J1655-40 as the reference correlation curve for estimating mass of IGR J17091-3624. This correlation was successfully used in ST07 to predict the mass of GRS 1915+105, a source with a very similar correlation curve to IGR J17091-3624. We keep the value of D fixed at 1.0 as done in ST07. We note though, that changing the value of D changes the final value of mass by a small amount. The best fitted curve (for D = 1.0) using Eqn. 1 is shown in Fig. 1 along-with the residuals (bottom panel). This fitting has been done using Craig Markwardt’s IDL based routines<sup>6</sup> (Markwardt 2009), suitably modified for accommodating errors in both variables, as is explained further in Appendix I. This fitting gives us values as  $A = 2.38_{-0.09}^{+0.05}$ ,  $B = 0.23_{-0.03}^{+0.02}$  and  $\nu_{tr} = 4.47_{-0.87}^{+0.64}$  Hz. The best fit mass (as obtained by scaling the B parameter with GRO J1655-40’s mass which is taken to be  $6.3 \pm 0.5 M_\odot$  (Green et al. 2001)) comes as  $M_{bh} = 10.90_{-1.48}^{+1.67} M_\odot$  with a fit statistic

<sup>6</sup> <http://purl.com/net/mpfit>

**Table 1**  
Reconditioning of reduced spectral data-sets

Instrument	Binning	Systematic error
<i>Swift</i> XRT	Minimum 20 counts per bin	3%
<i>INTEGRAL</i> IBIS/ISGRI	25 bins between 13 keV – 150 keV <sup>a</sup>	5%
<i>RXTE</i> PCA	None	0.5%

<sup>a</sup> IBIS/ISGRI has Gaussian distributed errors and doesn't need rebinning for noise statistics. By default 11 bins are present between 13 keV – 150 keV.

(Appendix I) of  $\mathcal{O} = 16.964$  for 18 degrees of freedom.

### 3.2. QPO frequency ( $\nu$ ) - Time (day) evolution

We model the monotonic increase in QPO frequencies with time using the Propagating Oscillatory Shock (POS) model (Chakrabarti & Manickam 2000, hereafter CM00; Chakrabarti et al. 2008). This model which comes under the TCAF paradigm, explains formation of QPOs due to an oscillating shock front formed in the sub-Keplerian component of the flow. The shock front starts to oscillate at infall time scales, where the infall time is the time taken by material parcel to fall onto the central source from the shock location. The reasons for shock oscillation can be either resonance oscillations, when the infall time scale is comparable to the cooling time scale of the Comptonizing post-shock region (Molteni et al. 1996), or unstable perturbations occurring in the shocked flow due to its viscosity (Lee et al. 2011; Das et al. 2014). The frequency of the QPO, which is the rate at which the shock front oscillates (Chakrabarti & Manickam 2000; Chakrabarti et al. 2008, 2009; Nandi et al. 2012; Radhika & Nandi 2014) is given as :

$$\nu(r_s) = \frac{\nu_{s0}}{2\pi R r_s \sqrt{r_s - 1.0}}, \quad (2)$$

where,  $r_s$  is the location of the drifting shock front,  $\nu_{s0}$  is the inverse of light-travel time across the black hole, given as  $\nu_{s0} = \frac{c}{r_g}$  and  $R$  is the compression ratio (i.e., ratio of post-shock to pre-shock densities of the flow). In Eqn. 2, we have introduced an additional  $2\pi$  factor in the denominator to ensure that the entire axisymmetric shock front region ( $2\pi r_s$ ) is oscillating in-phase and this is consistent with the hydrodynamic simulations of Molteni et al. (1996). The shock front drifts inward with a constant velocity  $v_0$  giving,

$$r_s(t) = r_{s0} \pm v_0 \left( \frac{t - t_0}{r_g} \right); \quad r_s > r_{s,min}, \quad (3)$$

$$r_s(t) = r_{s,min}; \quad \text{otherwise}, \quad (4)$$

where  $r_{s0}$  is the initial shock location at  $t_0$  (1<sup>st</sup> day of the outburst). We think that the observed flattening/saturation of QPO frequencies (see Figure 2) may be due to the fact that the oscillating shock front stops drifting further inward. We account for this in the equation by using a minimum shock location  $r_{s,min}$ .

We do the QPO evolution fitting by again using Markwardt's IDL routines<sup>6</sup>. The difference between our attempt and previous studies of the POS model (Chakrabarti et al. 2008, 2009; Nandi et al. 2012) is that

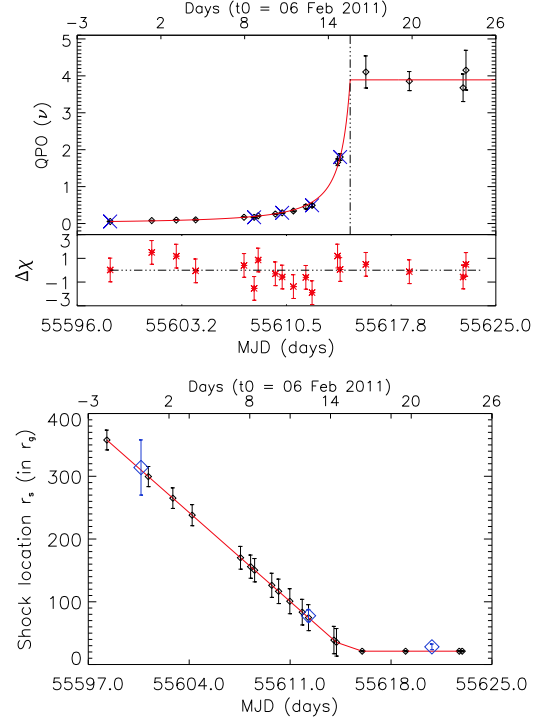


**Figure 2.** Evolution of QPO frequencies with time (days) of the onset-phase of the 2011 outburst of IGR J17091-3624 is fitted with POS model solution (top panel). Marked points (with cross) in top panel are *Swift* XRT QPOs. The corresponding size of the oscillating region is shown in the bottom panel with diamonds (blue) showing the ‘Compton cloud’ size as determined from spectral modelling (see §3.3). The best fit curve (red solid line) of Eqn. 2 to 4 gives an estimate of mass to be  $14.37_{-0.67}^{+0.71} M_{\odot}$ .

we have used mass as a free parameter. Most of the published work before this has dealt with establishing the POS model for sources of known mass by demonstrating that the QPO evolution can indeed be explained using the simple parametric expression in Eqn. 2. In our current implementation, the Schwarzschild radius  $r_g$  which is proportional to the mass of the source is used in the fitting function (Eqn. 2-4), as a free parameter. Hence mass is calculated by determining  $r_g$ . The other free parameters in the fitting are  $r_{s0}$  (the initial shock location) and  $r_{s,min}$ . The first day of the outburst ( $t_0$ ) is set from observations at 06 Feb 2011 (MJD 55598.28).  $R$  is held fixed at 3.0 and  $v_0$  at 10 m/s, which are typical values for these parameters. This is inferred from the fact that the shock front oscillates to give a detectable QPO for  $R$  between 2.0 and 4.0 (Nandi et al. 2012). The typical inward drift velocity of this front as obtained from previous studies lies between 5 – 15 m/s (Chakrabarti et al. 2008, 2009; Nandi et al. 2012; Radhika & Nandi 2014). We use the mean of these ranges in our fitting and inves-

tigate the effects of variation of  $R$  and  $v_0$  in the discussion section.

The results of the POS model fitting is shown in Figure 2 along with residuals (bottom panel of the top figure). The bottom figure shows the variation of the Comptonizing region (i.e., the size of the oscillating region) which decreases as the QPO frequency increases with time. The dashed dotted vertical line marks the transition of hard-intermediate to soft-intermediate state (Iyer & Nandi 2013), where photon index saturates over QPO frequency (see Fig. 2 and Fig. 1). We obtain the fitted value of the mass to be  $M_{bh} = 14.37_{+0.71}^{-0.67} M_{\odot}$  with  $\chi^2_{red} = 1.03$  ( $\chi^2/dof = 15.43/15$ ).

### 3.3. Spectral modelling based on TCAF

The spectral modelling is based on steady state hydrodynamic solutions of the equations governing the flow of accreting material under the TCAF paradigm. The solution for a set of free parameters gives a model spectrum, which we use to compare and fit the observed spectrum. We have incorporated the TCAF model (Chakrabarti & Titarchuk 1995; Chakrabarti & Mandal 2006; Mandal & Chakrabarti 2010) in XSPEC as a local model (Arnaud 1996) to achieve this spectral fitting. In this model, we consider a sub-Keplerian flow of accretion rate  $\dot{m}_h$  on the top of a Keplerian flow of accretion rate  $\dot{m}_d$  at the equatorial plane. Both the accretion rates are measured in units of the Eddington accretion rate ( $\dot{m}_{Edd}$ ). The other free parameters are mass of the central object ( $M_{bh}$ ), shock location ( $r_s$ ) and compression ratio ( $R$ ). A similar implementation in validating the TCAF model for a few black hole sources has been carried out by Debnath et al. (2014). But these previous studies are limited within 3.0 keV – 30.0 keV whereas in the current work we model the broadband spectrum between 0.5 keV – 100 keV.

To implement the local model in XSPEC, we use the HEASoft facility to create a table model by generating the model spectra for a large range of input parameters and saving it in an array. This table model can be run from XSPEC (XSPEC User's Guide) to calculate the fitting parameters. However, the values of the fit parameters so obtained may not be very accurate as XSPEC does an interpolation to fit the data. Hence, we have done the spectral modelling in two steps. First, we use the table model to constrain the parameters in reasonably narrow interval and then we run the actual hydrodynamic source code from XSPEC with the parameters previously obtained narrow interval to get the best fit.

During the 2011 outburst, the source evolved from hard to soft state via intermediate states. We have fitted the broadband spectra (0.5 - 100.0 keV) for all the observations where we could find simultaneous or quasi-simultaneous broadband observations. The observations so found lie in each of these spectral states: hard state (HS) observed on 08 Feb, hard intermediate (HIMS) on 20 Feb, Intermediate state near transition from HIMS to SIMS on 22 Feb, soft intermediate (SIMS) on 28 Feb, Intermediate state near transition from SIMS to SS on 08 Mar and soft state (SS) on 12 Mar (see Iyer & Nandi 2013). We model these six spectra by using our local TCAF model alongwith *phabs* model of XSPEC to account for the interstellar absorption. In the model spectrum

computation, the soft photons are supplied by the Keplerian disk and are inverse-Comptonized by hot electrons in the post-shock region. Hence, the resultant spectrum is a combination of soft and the hard components and the relative normalization is determined by the fraction of photons intercepted by the post-shock region. We finally fit the resultant spectra with observed spectra as shown in Fig. 3. The TCAF model fitted parameters are presented in Table 2. We have kept the compression ratio fixed ( $R=3$ ) for all spectral fitting. We see that as the source moves to soft state, the shock front moves inward and  $\dot{m}_d$  increases while  $\dot{m}_h$  decreases except for observations near the state transition boundaries (see §4 for details). This means that in the soft state, a lot more soft photons come from Keplerian disk and there exist lesser number of hot electrons to cool down. This is consistent with the physical picture of an accreting black hole source (Chakrabarti & Titarchuk 1995; Smith et al. 2001, 2002; Chakrabarti & Mandal 2006; Mandal & Chakrabarti 2010).

In our spectral fitting, we find that the column density ( $n_H$ ) varies between  $(0.97 - 1.7) \times 10^{22} \text{ cm}^{-2}$  while the source transits from the hard to the soft state. A higher value of  $n_H$  in the soft state may be due to enhanced disk winds (see King et al. 2012) or other sources of opacity. In our present work, we do not assume any distance to the source. We calculate the overall normalization parameter (fixed for all spectral fits) from our spectral modelling. For every data-set, we calculate the normalization constant associated with the best fit and then take an average over all normalizations from individual data-sets. Finally, we fit all the data-sets again with this new averaged normalization constant. Also, we do check that the final estimation of mass from individual data-sets with fixed overall normalization lies within the range of mass as determined by the individual normalization before taking the average. The overall normalization depends on the distance to the source and inclination angle of the system. The reported distance to the source and its inclination angle varies between 10 - 20 kpc (Altamirano et al. 2011; Rao & Vadawale 2012) and  $50^\circ$  -  $70^\circ$  (King et al. 2012) respectively. Hence for an inclination angle in the range ( $50^\circ$  -  $70^\circ$ ), the final normalisation constant translates into a distance range (10.6 - 14.6) kpc. For lower values of inclination angle, the distance to the source reduces even further. This suggests that the source flux is low, not due to the source being located at a very large distance. The spectral fitting gives a mass estimate as listed in the last column of Table 2, with  $\chi^2_{red}$  ( $\chi^2/dof$ ) for different states as 160.57/157 (HS), 132.85/158 (HIMS), 238.98/269 (HIMS-SIMS), 117.53/138 (SIMS), 341.85/283 (SIMS-SS) and 163.83/176 (SS) respectively.

## 4. DISCUSSION AND CONCLUSIONS

In this paper, we have tried to constrain the mass of IGR J17091-3624 by attempting to explain the X-ray spectral and timing observations under the TCAF paradigm. We find that the source behaviour can be consistently explained if the source mass is  $\gtrsim 10 M_{\odot}$ . To quantify this further, we first examine the limitations on each of our methods one by one. Finally, we attempt to put a single set of limits on the source mass from the different estimates presented in this paper. The summary

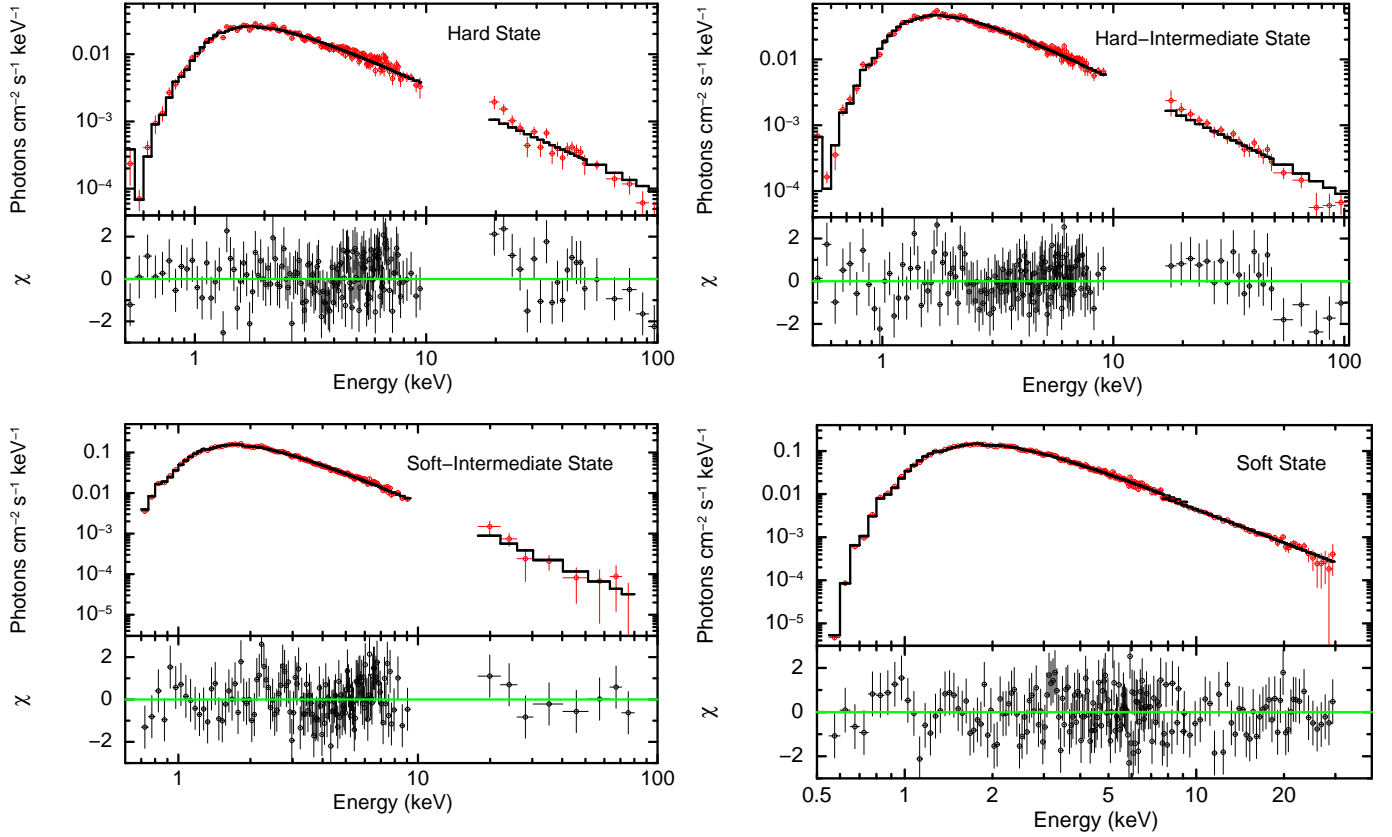


**Figure 3.** Broadband energy spectra fitted by TCAF model for different states mentioned on the respective figures (residuals are shown in bottom panels). HS, HIMS and SIMS spectra are taken by using simultaneous data from *Swift* XRT and *INTEGRAL* IBIS. SS spectrum is taken by using simultaneous data from *Swift* XRT and *RXTE* PCA. The fit parameters along with the estimated mass are presented in Table 2.

**Table 2**  
Results of the fitting for Mass estimation

Method	Details and Assumptions			Mass estimate
(A) $\Gamma$ - $\nu$ Correlation	See ST07			$10.90^{+1.48}_{-1.67} M_{\odot}$
(B) QPO Evolution (POS model)	See CM00, Nandi et al. (2012)			$14.37 \pm 0.67 M_{\odot}$
(C) Spectral Modelling (TCAF)	State	Shock location ( $r_s$ )	Accretion rate ( $\dot{m}_h, \dot{m}_d$ )	Mass ( $M_{\odot}$ )
	...			
	HS	$314 \pm 44$	$0.66 \pm 0.04, 0.08 \pm 0.01$	$12.7 \pm 0.6$
	HIMS	$77.3 \pm 9.3$	$0.58 \pm 0.04, 0.12 \pm 0.02$	$10.7 \pm 0.5$
	HIMS-SIMS	$35.1 \pm 11.3$	$0.16 \pm 0.015, 0.21 \pm 0.14$	$11.5 \pm 1.5$
	SIMS	$28.2 \pm 4.5$	$0.28 \pm 0.05, 0.63 \pm 0.08$	$12.9 \pm 1.1$
	SIMS-SS	$24.0 \pm 11.6$	$0.12 \pm 0.02, 1.09 \pm 0.09$	$13.1 \pm 1.1$
	SS	$19.0 \pm 3.7$	$0.25 \pm 0.06, 0.64 \pm 0.12$	$13.1 \pm 1.6$
Final Bounded Mass	Joint Likelihood : $11.8 M_{\odot} - 13.7 M_{\odot}$			

of mass estimates by *Photon Index* ( $\Gamma$ ) - *QPO frequency* ( $\nu$ ) *correlation*, *QPO frequency* ( $\nu$ ) - *Time (day) evolution* and *Spectral modelling based on TCAF* is given in Table 2.

In the  $\Gamma$ -QPO correlation model, we have noted that our inferred value of mass depends on the value of ‘D’ parameter. In this method, we find that the range of frequency over which the transition (bottom left to top right) in the correlation curve (see Fig. 1) occurs for the reference source of our choice, GRO J1655-40 ( $\sim 0.1$  Hz to 15 Hz), is about three times the range for IGR J17091-

3624 ( $\sim 0.05$  Hz to 5 Hz). This would give us an estimate of  $D=0.33$ , obtained as a ratio of the frequency range of the two sources, as D controls the range of frequencies over which the correlation curve shows the above mentioned transition. However, we also note that the value of  $D = 1.0$  is used to scale the mass of GRO J1655-40 to GRS 1915+105 (see ST07 for details). GRS 1915+105 has a similar span of QPO frequencies like IGR J17091-3624. To resolve this, we redo the fit for different values of parameter D from 0.33 to 1.0, and note the variation in mass as the uncertainty / limitation of this model.



We find that the mass estimate shifts from a minimum at  $9.50 M_{\odot}$  to a maximum of  $10.90 M_{\odot}$ . The value of  $1.4 M_{\odot}$  ( $10.9 M_{\odot} - 9.5 M_{\odot}$ ) is total uncertainty on the estimated mass using this method. To use this uncertainty in our final estimate, we take the  $1\sigma$  uncertainty to be one third of this value (i.e., we take  $1.4 M_{\odot}$  to encompass  $3\sigma$  (or 99%) of the total uncertainty of this method). The scaling law used to obtain the mass from this method is based on the model of Titarchuk & Fiorito (2004) and the empirical relation of ST07. If this empirical relation and the subsequent linear scaling mis-specify the actual physical relation involved, then that could introduce another source of uncertainty in this estimate (see Yang et al. (2012) to get an idea of model uncertainties due to mis-specified scaling assumptions). We do not explicitly account for this in our paper, as further investigation of this model would require cross validating the model against multiple black hole systems with a large sample of data (see Kessler et al. (2013) for an example of uncertainty estimation).

In the QPO evolution model, we see that the the range of values over which  $R$  and  $v_0$  can potentially vary adds a source of uncertainty to our quoted values of mass. As done above, we try to estimate this by redoing the QPO evolution fit for different  $R$  (from 2.0 to 4.0) and  $v_0$  (from 5 m/s to 15 m/s). We find that this gives an uncertainty in mass of  $1.7 M_{\odot}$  from the mean value (i.e., the standard deviation ( $1\sigma$ ) in the final set of mass values is  $1.7 M_{\odot}$ ). Secondly, and more importantly, the data does not fit well if  $v_0$  is less than 8 m/s or greater than 12 m/s. In a recent paper, Mondol et al. (2015) have mentioned that the velocity of propagation of the shock front can be calculated from spectral modelling by estimating the shock location. However, in the present paper we treat spectral modelling and QPO frequency modelling as two independent methods and hence do not use the results from one method in the other method.

The spectral fitting method under TCAF paradigm also has a few limitations as listed below. Our spectral modelling includes black body and inverse-Comptonization components. These two components are good enough to fit the spectra of IGR J17091-3624. But there are other sources where these two components are not sufficient and we need to include components like a Gaussian emission line profile (e.g. GRS 1915+105), and absorption smear edges (e.g. XTE J1859+226). We need to include other physical processes in our model to generate such components. The hydrodynamic solutions used to calculate the model spectra are not self-consistent transonic solutions. The number of fit parameters can be reduced further if we use transonic solutions. To account for the shock transition from pre-shock to post shock region, we fix the value of  $R = 3.0$  (as done in §3.2). We find that spectral modelling is not very sensitive to  $R$  in our case and do not account for it separately. Secondly, an uncertainty in overall normalization (fixed for all data-sets) may lead to the uncertainty in the estimated mass. Our spectral modelling constrains the system in such a manner, that we address the spectral shape along with the overall luminosity simultaneously for multiple data-sets. In principle, we do not expect the normalization to change across data-sets. Hence, we expect this uncertainty to be small enough to not significantly affect the

mass estimation.

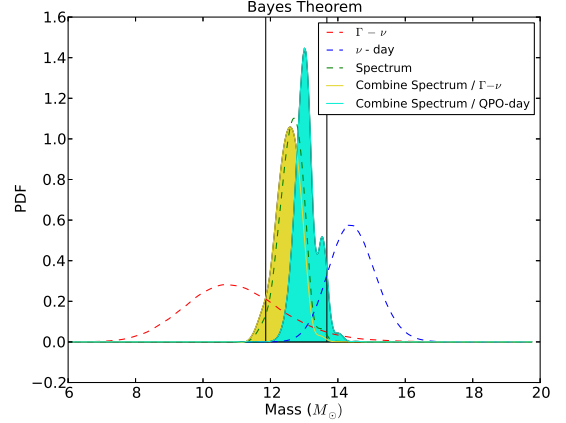


**Figure 4.** Combining the estimates. Figure shows the results from the joint likelihood based approach for combining the mass estimates. See Appendix II and Appendix III for details.

Given these three estimates and considering the limitations of the methods, we try to combine the results to get the overall range of mass of the object. For combining the estimates, we calculate the probability distribution function (PDF) of the mass of the central object from the least-squares fit for each method (see Appendix II). We combine results from the independent methods only. Thus, we do not combine the results from  $\Gamma - \nu$  correlation and from QPO-day variation, since both these methods share the common variable  $\nu$  (the QPO frequency). Instead we combine results from §3.1 with results from §3.3, and results from §3.2 with results from §3.3 separately. Finally, we quote the lowermost and uppermost values from such a combination as the final mass bound. The approach that we take to combine the estimates is based on estimation of joint likelihood using the Naive Bayes theorem from independent PDFs (see Appendix III for details). We present the combined estimate in Figure 4, where red, blue and green lines are individual PDFs from §3.1, §3.2 and §3.3 respectively. The combined estimates are represented by shaded regions. The combined estimate using this approach for §3.1 – §3.3 gives us a mass range of  $11.8 M_{\odot} - 13.1 M_{\odot}$  and for §3.2 – §3.3 gives us a mass range of  $12.5 M_{\odot} - 13.7 M_{\odot}$ . This gives us a limit on the black hole mass of  $11.8 M_{\odot} - 13.7 M_{\odot}$ . For a worst case estimate, we find the 90% confidence value limits for each estimate from its respective PDF. The lowermost and uppermost of these limits places the mass between  $8.7 M_{\odot} - 15.6 M_{\odot}$ .

Whichever way we combine the estimates, we see that the mass is greater than  $8.7 M_{\odot}$ . This suggests that IGR J17091 also harbours a black hole with mass similar to the black hole of GRS 1915+105 (see Reid et al. 2014, for a recent mass estimate). The reason for any distinction between these two sources, may then be the difference in mass accretion rates. For IGR J17091-3624, we obtain the total mass accretion rate to be in the range (0.4 - 1.1) times the Eddington accretion rate (see Table 2). We obtain near-Eddington accretion rate close to the transition from SIMS to Soft State and lowest

accretion rate near the transition from HIMS to SIMS (Iyer & Nandi 2013). We note that the non-simultaneous nature of the spectra in these two observations with a gap of  $\sim 6$  hours may have contributed to this. This may also be due to many other time dependent nonlinear effects (for e.g. flow viscosity (Mandal & Chakrabarti 2010), or jet activity (Radhika & Nandi 2014)) involved in the system during the state transitions. Our spectral fitting is done by using a steady state model and does not account for these time varying phenomena. We have attempted to apply our spectral modelling techniques on GRS 1915+105 as well for a relative comparison of flow accretion rate. While modelling the  $\chi$  class spectrum of GRS 1915+105, we find evidence for super-Eddington accretion rates ( $\sim 6.5$  times the Eddington accretion rate) in the system. In future, we would like to do a detailed broadband spectral modelling of different variability classes of GRS 1915+105 and IGR J17091-3624 to make a comparative study of the variation in accretion rate in both systems. However, it is suggestive to note that the difference in accretion rates, could be the reason for the observed difference in X-ray flux.

If that indeed is the case, then it raises the question of how both sub- and super-Eddington accretion rates give rise to similar kinds of multiple variability classes as seen in these objects. It is possible that the complex variability classes observed in these sources (IGR J17091-3624 & GRS 1915+105) could be due to the interplay between the Keplerian and sub-Keplerian flows in presence of outflows/winds in the soft-intermediate state (Chakrabarti & Titarchuk 1995; Chakrabarti & Nandi 2001; Mandal & Chakrabarti 2010). As seen from Table 2, the intermediate states have comparable values of sub-Keplerian ( $\dot{m}_h$ ) and Keplerian ( $\dot{m}_d$ ) accretion rates, which can be due to the conversion of one type of matter flow into the other type (Mandal & Chakrabarti 2010). Accordingly, a super-Eddington accretion rate may not be a pre-requisite for these variability classes to occur.

The interplay between the different accreting (Keplerian and sub-Keplerian) matter with the outflowing matter may itself cause such variabilities. It is possible that such an interplay between the accreting and outflowing streams is currently happening in GRS 1915+105 and that in the past this system too might have undergone an evolution from the Hard to the Intermediate states to its present phase like other such sources (see Nandi et al. (2012) for GX 339-4 and Capitanio et al. (2012) for IGR J17091-3624).

Details of such similarities between the variability classes in GRS 1915+105 and those observed in other such sources will be explored later and presented elsewhere. Until we know a concrete explanation for the occurrence of such variability classes, concluding on the nature of sources showing such variabilities is difficult. However, our current work suggests the presence of a high mass stellar black hole in the binary system IGR J17091-3624, which accretes at sub-Eddington rates and still shows such variability classes.

This research has made use of data obtained through the High Energy Astrophysics Science Archive Research Center (HEASARC) online service, provided by the NASA/Goddard Space Flight Center. We thank Prof. Belloni and Prof. Markwardt for making their codes (GHATS and MPFIT) available. We thank Prof. A. R. Rao, TIFR and Dr. Seetha, Space Science Office, ISRO-HQ for useful suggestions. We thank Dr. Kim Page of the *Swift* team for prompt and continued help in the analysis of *Swift XRT* data. We thank Dr. Sankar, ISAC, Prof. T. Krishnan (retd.) and Prof. M. Delampady, ISI for their help and suggestions with error analysis and statistics. We thank Dr. Anil Agarwal, GD, SAG; Mr. Vasantha E. DD, CDA and Dr. S. K. Shivakumar, Director, ISAC for encouragement and continuous support to carry out this research. Finally, we would also like to thank anonymous referees for their useful suggestions to improve the manuscript.

## APPENDIX

### APPENDIX I : FITTING WITH ERRORS IN TWO VARIABLES

This gives a brief outline of the error in variable method, and the technique that we have used here. For further details, please refer to Macdonald & Thompson (1992); Press et al. (1992, and references therein). One way to accommodate errors in the second variable is to alter the fit statistic used for minimization. Various formulations are discussed in Macdonald & Thompson (1992), but we use the one (denoted here as  $\mathcal{O}$ ) and given as

$$\mathcal{O}^2 = \sum_{i=0}^N \frac{(y_i - f(x_i))^2}{\text{var}(y_i - f(x_i))}.$$

For estimating confidence intervals on the mass, we do Monte Carlo runs of the same fitting routine with the observations  $(x_i, y_i)$  randomly generated as per their error variance (see Press et al. 1992, for details). We then use a Gaussian kernel density estimator to find the probability density function of the obtained set of mass values. The errors on the final set of parameters are quoted as  $1\sigma$  (68%) deviations from their central value.

### APPENDIX II : PDF CALCULATION FOR THE METHODS MENTIONED IN §3.1 - §3.3

This section gives an outline of the methods used to construct a PDF from the results of the statistical fitting routines.

- Construct PDF for §3.1

The PDF is obtained by doing Monte-Carlo simulation runs on the data. We simulate multiple data-sets ( $\sim 10^5$ ) from the assumed Gaussian error distributions on photon index ( $\Gamma$ ) and QPO frequency ( $\nu$ ) (Appendix I). For



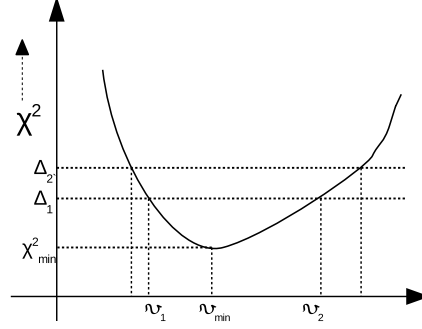


**Figure 5.** Chi-square variation plot of parameter ( $v$ ) used to obtain the PDF. Plot shows different levels of  $\chi^2$ , namely  $\Delta_1$  at which the confidence levels and the confidence intervals ( $v_1, v_2$ ) are estimated. The PDF is calculated from these confidence levels.

each simulated data-set we repeat the least squares fitting routine and note the parameter and statistic value. Finally, we obtain a distribution of our parameter of interest (i.e., Mass) by using a Gaussian Kernel Density Estimator.

- Construct PDF for §3.2 and §3.3

The PDF is obtained from the variation of the fit-statistic (chi-square) about the parameter minima. This gives the confidence intervals ( $v_1, v_2$ ) on a single parameter from the least-squares fit as seen in equation below

$$C_{v_1}^{v_2} = \int_{v_1}^{v_2} p(v)dv = P(\chi^2 > \Delta_1).$$

Here,  $\chi^2$  denotes the chi-squared distribution with 1 degree of freedom,  $p(v)$  denotes the PDF of parameter  $v$ ,  $C_{v_1}^{v_2}$  denotes the confidence level and  $\Delta_1$  is the level (corresponding to  $v_1$  and  $v_2$ ) of variation in the  $\chi^2$  statistic (see Figure 5 for details).

These confidence levels are taken to be the representative areas under the PDF curve in the given interval ( $v_1$  to  $v_2$ ). We find the half area (denoted as  $A$ ) under the PDF curve from each side of the interval ( $v_1$  or  $v_2$ ) to the minimum value ( $v_{min}$ ) by

$$A_{v_1}^{v_{min}} = \frac{v_{min} - v_1}{v_2 - v_1} C_{v_1}^{v_2} ; A_{v_{min}}^{v_2} = \frac{v_2 - v_{min}}{v_2 - v_1} C_{v_1}^{v_2}.$$

This is applied to  $\Delta_1$  which is closest to  $v_{min}$ . For subsequent  $\Delta$  and  $v$ , we find the corresponding half areas ( $A$ ), by cumulatively adding to the previous estimate of half area ( $A$ ). Thus, we bin the  $\Delta$  values in small steps to estimate these half areas for many points. From these half areas ( $A$ ), the Cumulative Density Function (CDF) for each distribution can be found as,

$$F(v) = \int_{-\infty}^v p(v)dv = \begin{cases} A_{-\infty}^{v_{min}} - A_{v_{min}}^v, & v < v_{min} \\ A_{-\infty}^{v_{min}} + A_{v_{min}}^v, & v > v_{min} \end{cases}.$$

Once, we obtain the CDF, the PDF can be calculated by taking a derivative of this, which can be written as :

$$p(v) = \frac{d}{dv} F(v).$$

### APPENDIX III : COMBINING THE ESTIMATES

The combination of estimates can be done using the likelihood  $P(M_i|X_i)$ , which denotes the PDF of mass from observations  $X_i$  of method  $i$  (see Appendix II for details on estimation of the PDF). We follow the approach as explained below to find the combined / overall limits of the mass from independent PDF only. Thereby, we combine the estimate in §3.1 with §3.3 and §3.2 with §3.3 separately.

- Joint Likelihood estimation using the Naive Bayes theorem

The joint likelihood of the three methods for BH mass estimation can be obtained using the simple procedure known as the ‘naive Bayes’ algorithm where

$$P(M) = K \prod P(M_i|X_i).$$

The Naive Bayes approach has been used commonly for multivariate classification of objects like stars in catalogs (see Broos et al. 2013). We use it here, for parameter confidence level estimation. Here,  $P(M)$  denotes the combined / final PDF of mass and  $K$  is the normalization constant to get unit area PDF. This method, when applied to Gaussian distributions gives exactly the weighted average estimate, where the mean of the joint PDF will give the weighted average and the standard deviation of the joint PDF will give the error on the weighted average. Thus, in this method the width of the final PDF is always less than that of each individual PDF. However, this method can only be applied to PDFs which are independent to each other. In classification schemes, usage of the Naive Bayes approach has shown to give acceptable results even if independence is violated, as is shown in Domingos & Pazzani (1997). In our case, if dependence among our mass estimation methods exists and is not accounted for, leads to underestimation of the width of the final PDF. To overcome this, we do not combine the PDFs from the methods which may have some level of dependence. Another limitation of this method is that it gives an offset / biased PDF, if any of the individual PDFs have unaccounted biases / systematics. To calculate the joint PDF we perform a multiplication of the individual PDFs for every value of mass in the range from  $6 M_{\odot}$  to  $20 M_{\odot}$ .

Once we obtain the final PDF  $P(M)$ , we quote the confidence interval of the mass by finding the limits beyond which the PDF encompasses 5% of the distribution on each side, i.e., we compute  $M_1$  and  $M_2$  to give  $P(M < M_1) = P(M > M_2) = 0.05$ . Thus, we find the 90% confidence interval on the mass. We note that this interval may extend to a smaller level of confidence than 90% due to an increase in the width of the combined PDF in case of unaccounted dependence between the individual PDFs.

## REFERENCES

- Agrawal, V. K., & Bhattacharyya, S., 2003, *A&A*, 398, 223  
 Altamirano, D., Belloni, T., Linares, M., et al. 2011, *ApJ*, 742, L17  
 Altamirano, D., & Belloni, T. 2012, *ApJ*, 747, L4  
 Arnaud, K. A. 1996, in *ASP Conf. series*, Vol. 101, *Astronomical Data Analysis Software and Systems V*, ed. G. Jacoby & B. J., 17  
 Belloni, T., Klein-Wolt, M., Méndez, M., van der Klis, M., & van Paradijs, J. 2000, *A&A*, 355, 271  
 Bodaghee, A., Rahoui, F., Tomsick, J. A., & Rodriguez, J. 2012, *ApJ*, 751, 113  
 Broos, P. S. and Getman, K. V. and Povich, M. S. and Feigelson, E. D. and Townsley, L. K. and Naylor, T. and Kuhn, M. A. and King, R. R. and Busk, H. A., 2013, *ApJS*, 209, 32  
 Cambier, H. J., Smith, & D. M., 2013, *ApJ*, 767, 46  
 Capitanio, F., Bazzano, A., Ubertini, P., et al. 2006, *ApJ*, 643, 376  
 Capitanio, F., Del Santo, M., Bozzo, E., et al. 2012, *MNRAS*, 422, 3130  
 Chakrabarti, S., & Titarchuk, L. G. 1995, *ApJ*, 455, 623  
 Chakrabarti, S. K., & Manickam, S. G. 2000, *ApJ*, 531, L41  
 Chakrabarti, S. K., & Nandi, A., 2001, *Ind J. Physics*, 75B(1), ArXiv e-prints, arXiv:0012526  
 Chakrabarti, S. K., & Mandal, S. 2006, *ApJ*, 642, L49  
 Chakrabarti, S. K., Debnath, D., Nandi, A., & Pal, P. S. 2008, *A&A*, 489, L41  
 Chakrabarti, S. K., Dutta, B. G., & Pal, P. S. 2009, *MNRAS*, 394, 1463  
 Das, S., Chattopadhyay, I., Nandi, A., & Molteni, D. 2014, *MNRAS*, 442, 251  
 Debnath, D., Chakrabarti, S. K., & Mondal, S., 2014, *MNRAS*, 440, L121  
 Domingos, P., & Pazzani, M., 1997, *Machine Learning*, 209, 103  
 Green, J., Bailyn, C. D., & Orosz, J. A. 2001, *ApJ*, 554, 1290  
 in't Zand, J. J. M., Heise, J., Lowes, P., & Ubertini, P. 2003, *Astron. Telegram*, 160, 1  
 Iyer, N., & Nandi, A. 2013, in *ASInC*, ed. S. Das, A. Nandi, & I. Chattopadhyay, Vol. 8, 79–83  
 Kessler, R., Guy, J., Marriner, J., et al., 2013, *ApJ*, 764, 48  
 King, A. L., Miller, J. M., Raymond, J., et al. 2012, *ApJ*, 746, L20  
 Lebrun, F., et al., 2003, *A&A*, 411, 141  
 Lee, S.-J., Ryu, D., & Chattopadhyay, I. 2011, *ApJ*, 728, 142  
 Macdonald, J. R., & Thompson, W. J. 1992, *Am. J. Phys.*, 60, 66  
 Mandal, S., & Chakrabarti, S. K. 2010, *ApJ*, 710, L147  
 Markwardt, C. B. 2009, in *Astronomical Society of the Pacific Conference Series*, Vol. 411, *Astronomical Data Analysis Software and Systems XVIII*, ed. D. A. Bohlender, D. Durand, & P. Dowler, 251  
 Molteni, D., Sponholz, H., & Chakrabarti, S. K. 1996, *ApJ*, 457, 805  
 Mondal, S., Chakrabarti, S. K., & Debnath, D., 2015, *ApJ*, 798, 57  
 Nandi, A., Debnath, D., Mandal, S., & Chakrabarti, S. K. 2012, *A&A*, 542, A56  
 O'Neill, P. M., Kuulkers, E., Sood, R. K., & van der Klis, M., 2002, *MNRAS*, 336, 217  
 Pahari, M., Yadav, J. S., & Bhattacharyya, S. 2011, *ArXiv e-prints*, arXiv:1105.4694  
 Press, W. H., Flannery, B. P., Teukolsky, S. A., & Vetterling, W. T. 1992, *Numerical Recipes in C* (Cambridge University Press, 1992, 2nd ed.)  
 Radhika, D., & Nandi, A. 2014, *AdSpR*, 54, 1678  
 Rao, A., & Vadawale, S. V. 2012, *ApJ*, 757, L12  
 Rebusco, P., Moskalik, P., Kluźniak, W., & Abramowicz, M. A. 2012, *A&A*, 540, L4  
 Reid, M. J., McClintock, J. E., Steiner, J. F., Steeghs, D., Remillard, R. A., Dhawan, V., & Narayan, R., 2014, *ApJ*, 796, 2  
 Remillard, R. A., & McClintock, J. E. 2006, *ARA&A*, 44, 49  
 Revnivtsev, M., Gilfanov, M., Churazov, E., & Sunyaev, R. 2003, *Astron. Telegram*, 150, 1  
 Rodriguez, J., Corbel, S., Caballero, I., et al. 2011, *A&A*, 533, L4  
 Romano, P., Campana, S., Chincarini, G., et al., 2006, *A&A*, 456, 917  
 Shakura, N. I., & Sunyaev, R. A. 1973, *A&A*, 24, 337  
 Shaposhnikov, N. 2011, *Astron. Telegram*, 3179, 1  
 Shaposhnikov, N., & Titarchuk, L. 2007, *ApJ*, 663, 445  
 Shaposhnikov, N., & Titarchuk, L. 2009, *ApJ*, 699, 453  
 Smith, D. M., Dawson, D. M., & Swank, J. H. 2007, *ApJ*, 669, 1138  
 Smith, D. M., Heindl, W. A., Markwardt, C. B., & Swank, J. H. 2001, *ApJ*, 554, L41  
 Smith, D. M., Heindl, W. A., & Swank, J. H. 2002, *ApJ*, 569, 362  
 Titarchuk, L., & Wood, K., 2002, *ApJ*, 577, L23  
 Titarchuk, L., & Fiorito, R. 2004, *ApJ*, 612, 988  
 Wu, K., et al. 2002, *ApJ*, 565, 1161  
 Yang, H. -Y. K., Sutter, P. M., Ricker, P. M. 2012, *MNRAS*, 427, 1614  
 Zhang, W., Jahoda, K., Swank, J. H., Morgan, E. H., & Giles, A. B. 1995, *ApJ*, 449, 930